

University of Nebraska - Lincoln

DigitalCommons@University of Nebraska - Lincoln

Faculty Publications from the Department of
Electrical and Computer Engineering

Electrical & Computer Engineering, Department of

2019

Beam Manipulation Mechanisms of Dielectric Metasurfaces

Baoshan Guo

Beijing Institute of Technology

Lan Jiang

Beijing Institute of Technology, jianglan@bit.edu.cn

Yanhong Hua

Beijing Institute of Technology

Ningwei Zhan

Beijing Institute of Technology

Jingang Jia

Beijing Institute of Technology

See next page for additional authors

Follow this and additional works at: <https://digitalcommons.unl.edu/electricalengineeringfacpub>



Part of the [Computer Engineering Commons](#), and the [Electrical and Computer Engineering Commons](#)

Guo, Baoshan; Jiang, Lan; Hua, Yanhong; Zhan, Ningwei; Jia, Jingang; Chu, Kunpeng; and Lu, Yongfeng, "Beam Manipulation Mechanisms of Dielectric Metasurfaces" (2019). *Faculty Publications from the Department of Electrical and Computer Engineering*. 501. <https://digitalcommons.unl.edu/electricalengineeringfacpub/501>

This Article is brought to you for free and open access by the Electrical & Computer Engineering, Department of at DigitalCommons@University of Nebraska - Lincoln. It has been accepted for inclusion in Faculty Publications from the Department of Electrical and Computer Engineering by an authorized administrator of DigitalCommons@University of Nebraska - Lincoln.

Authors

Baoshan Guo, Lan Jiang, Yanhong Hua, Ningwei Zhan, Jingang Jia, Kunpeng Chu, and Yongfeng Lu

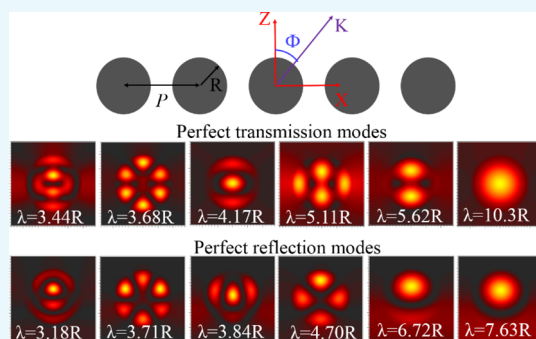
Beam Manipulation Mechanisms of Dielectric Metasurfaces

Baoshan Guo,[†] Lan Jiang,^{*†} Yanhong Hua,[†] Ningwei Zhan,[†] Jingang Jia,[†] Kunpeng Chu,[†] and YongFeng Lu^{†‡}

[†]Laser Micro/Nano Fabrication Laboratory, School of Mechanical Engineering, Beijing Institute of Technology, Beijing 100081, China

[‡]Department of Electrical Engineering, University of Nebraska-Lincoln, Lincoln, Nebraska 68588-0511, United States

ABSTRACT: Dielectric metasurfaces can achieve flexible beam manipulations. Herein, we study dielectric metasurfaces with different refractive indices, periods, incident angles, and cross-sectional shapes to determine the metasurface working mechanisms. Perfect transmission mainly depends on multipolar interference that can be used to control the transmission modes through the hybrid periods, hybrid cross sections, and multilayers. Perfect reflection is strongly influenced by the period of the metasurface and occurs only when the period is shorter than incident wavelength, which can be attributed to the lattice coupling. Furthermore, lattice coupling can be classified into two types with distinct properties: vertical mode and horizontal mode coupling. The vertical mode appears when the effective wavelength matches the feature size, whereas the horizontal mode only appears when the incident wavelength is close to the period. The horizontal mode is sensitive to the incident angle. The revealed functioning mechanisms enable further practical applications of metasurfaces.



The vertical mode appears when the effective wavelength matches the feature size, whereas the horizontal mode only appears when the incident wavelength is close to the period. The horizontal mode is sensitive to the incident angle. The revealed functioning mechanisms enable further practical applications of metasurfaces.

1. INTRODUCTION

Metasurfaces have been widely studied due to their abilities to modulate the behaviors of electromagnetic waves. The rapid development of metasurfaces has led to a number of applications, including nanoimaging, surface-enhanced spectroscopy, highly efficient holograms, photovoltaics, and quantum interferences in both linear and nonlinear regimes based on wavefront shaping and beam manipulation.^{1–14} However, controversies regarding the origin of metasurfaces still exist.^{10,15,16} Moreover, in many metasurface applications, the design mainly depends on the gradient structure, which can induce uneven phase distribution in space and can thus achieve different functions.^{17–21} Recently, the frequency-dependent transmission-type digital metasurface and low-profile planar coding antenna were proposed and demonstrated to control transmission/radiation waves.^{22,23} Nevertheless, gradient metasurfaces require fine discretizations of the structure to generate graded phase profiles, which makes it difficult to fabricate them. Increasingly complicated structures have been designed to manipulate optical beams with high efficiency.^{24–29} However, all these structures face similar manufacturing challenges.

To achieve flexible beam manipulation with high efficiency and low requirements for advanced manufacturing technology, dielectric metasurfaces utilizing multipolar interferences and diffractions are exploited, which could provide a new platform for further development of many branches of optics related to beam engineering.^{30–39} However, the basic physical mechanisms have not been clearly identified, although many groups have made contributions to mechanism investigations. Some researchers have focused on only the dipolar excitations and

have not established the links between multipolar interferences and beam controls.^{35–38,40} Others have considered high-order modes, such as electric quadrupole (EQ), electric octupole (EO), magnetic quadrupole, and magnetic octupole, but have not indicated their exact effects or working mechanisms for different phenomena.^{39,41–44} There exists a consensus that all demonstrated beam manipulations can be simply attributed to the interaction between lattice coupling and multipolar interference. However, how this interaction works and how it affects metasurface properties remain to be studied. In this paper, we numerically study the wave scattering of a one-dimensional (1D) metasurface (or metalattice) consisting of dielectric cylinders to detail the mechanisms and effects of lattice coupling and multipolar interference on metasurface properties.

2. SIMULATION RESULTS AND DISCUSSIONS

Figure 1a displays a schematic of the 1D metasurface consisting of periodic cylinders (with radius R and refractive index n). The cylinders can have cross sections of different shapes, such as a square or triangle (discussed later in this paper). The period (P) is along the X direction. The incident plane wave of the in-plane wavevector K (in the X – Z plane: $K \perp Y$) can be s-polarized (TE mode, electric field along Y direction: $E_0 \parallel Y$) or p-polarized (TM mode, magnetic field

Received: March 7, 2019

Accepted: April 15, 2019

Published: April 24, 2019

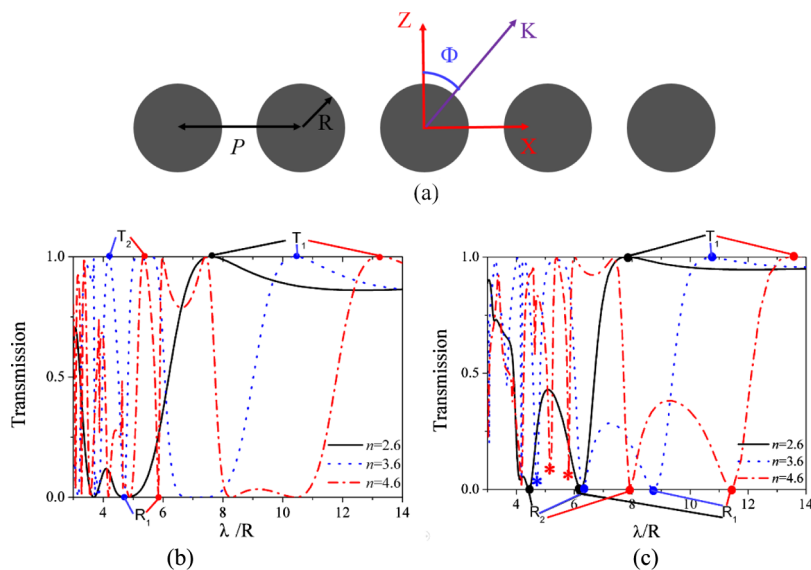


Figure 1. Schematic of dielectric grating with radius R and period P (a). The incident waves propagate along the direction of K with an incident angle of Φ . Transmission properties of the metasurface with different periods: (b) $P = 2.8R$, $n = 2.6$ (black solid line), $n = 3.6$ (blue dotted line), and $n = 4.6$ (red dash-dotted line); and (c) $P = 4R$, $n = 2.6$ (black solid line), $n = 3.6$ (blue dotted line), and $n = 4.6$ (red dash-dotted line).

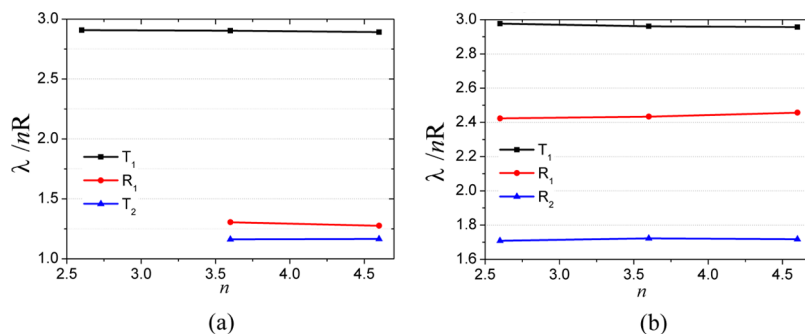


Figure 2. Effective wavelength of the transmission (T) peaks and reflection (R) peaks marked in Figure 1b,c for different n : (a) $P = 2.8R$, T_1 (black square line), T_2 (blue triangle line), and R_1 (red circle line) and (b) $P = 4R$, T_1 (black square line), R_1 (red circle line), and R_2 (blue triangle line).

along Y direction: $H_0 \parallel Y$). The plane wave has an incident angle of Φ and free-space wavelength of λ .

First, we analyze the scattering properties, including the perfect transmission and perfect reflection, of a single metasurface with p-polarized normally incident beam illumination. The transmission properties of such a metasurface with different periods (P) are illustrated in Figure 1b,c. For $P = 2.8R$ (Figure 1b), when the refractive index (n) equals 2.6 (black line), the figure reveals only one transmission peak and two reflection peaks in the wavelength range investigated. When n increases to 3.6 (blue dotted line), the figure reveals four transmission and four reflection peaks, and all the peaks are red-shifted. When n further increases to 4.6 (red dash-dotted line), the main transmission and reflection peaks are similar to those of $n = 3.6$; however, the positions of the corresponding peaks are shifted toward long wavelengths. Concurrently, there occur increased fluctuations in the short wavelength region. If the period (P) increases to $4R$ (Figure 1c), the trend is consistent. All the peaks are red-shifted with an increase in n . However, the reflection band displayed in Figure 1b degenerates into two reflection peaks, which is useful for wavelength-sensitive applications, and some new modes appear. When $n = 4.6$ (red dash-dotted line), two reflection peaks marked by red asterisks appear, one of which is the red

shift of the corresponding peak marked by a blue asterisk ($n = 3.6$), whereas the other peak is a new mode. The original single mode can be considered to be split into two modes.

As displayed in Figure 1b,c, for metasurfaces with periods of $2.8R$ and $4R$, the transmission or reflection peaks are linearly red-shifted as the refractive index (n) increases, which ensures that the effective wavelength remains unchanged (Figure 2). The effective wavelengths (λ/nR) at the transmission or reflection peaks marked by the red dots ($n = 4.6$), blue dots ($n = 3.6$), and black dots ($n = 2.6$) in Figure 1b,c are illustrated in Figure 2a,b, respectively. The transmission peaks T_1 (black square line) and T_2 (blue triangle line) and the reflection peak R_1 (red circle line) associated with different refractive indices (marked in Figure 1b) have an equal effective wavelength (Figure 2a). Similarly, the transmission peak T_1 (black square line) and the reflection peaks R_1 (red circle line) and R_2 (blue triangle line) marked in Figure 1c have an equal effective wavelength (Figure 2b). Therefore, the main effect of increasing the refractive index (n) is to increase the applicable wavelengths of the metasurface.

Next, we examine the effect of the period on transmission and reflection properties. For p-polarized (TM) incident plane waves (Figure 3a,c), as the period becomes larger, the perfect transmission peaks or perfect reflection peaks degrade,

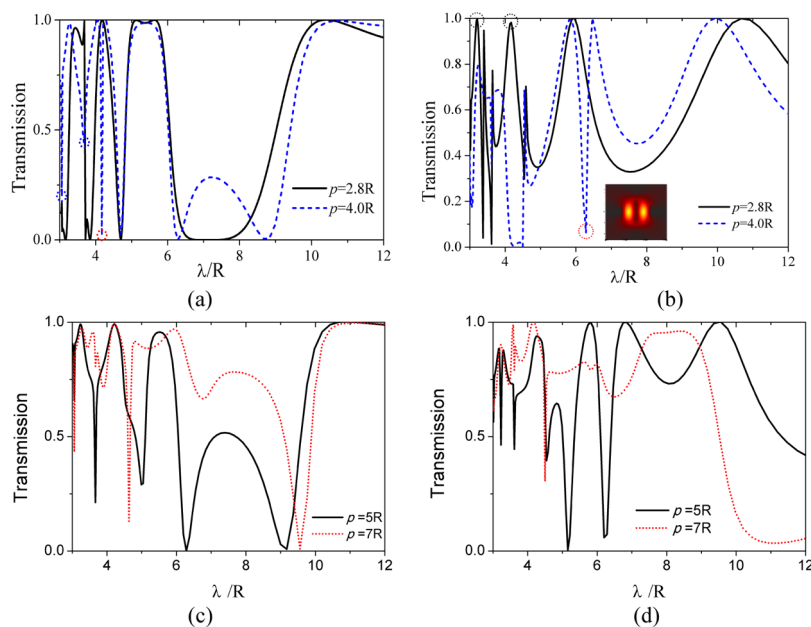


Figure 3. Transmission properties of p-polarized (TM) and s-polarized (TE) incident plane waves for different periods, where $n = 3.6$: (a) TM waves, $P = 2.8R$ (black solid curve) and $P = 4R$ (blue dashed curve); (b) TE waves, $P = 2.8R$ (black solid curve) and $P = 4R$ (blue dashed curve); (c) TM waves, $P = 5R$ (black solid curve) and $P = 7R$ (red dotted curve); and (d) TE waves, $P = 5R$ (black solid curve) and $P = 7R$ (red dotted curve).

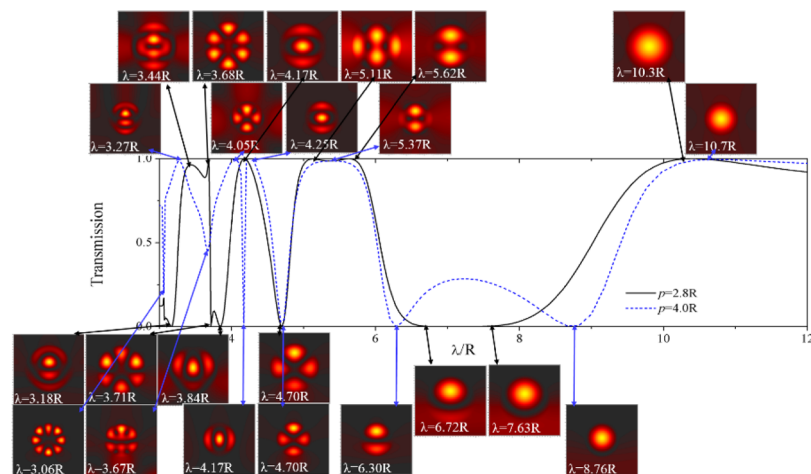


Figure 4. Optical patterns of light field distribution in the cylinders at each peak of different periods at $n = 3.6$ [black solid line ($P = 2.8R$); blue dashed line ($P = 4R$)]. The peak value is indicated in the corresponding mode patterns.

especially in the short wavelength region. This phenomenon occurs mainly because the optical field interaction between the cylinders (lattice coupling) becomes weak when the wavelength is less than the period. For example, for $P = 4R$ (blue dashed curve in Figure 3a), the two reflection peaks marked by the blue dashed circles in the short wavelength range ($\lambda < 4R$) degenerate compared with the situation when $P = 2.8R$ (black solid curve). Concurrently, a new reflection mode marked by a red dashed circle is generated at $\lambda = 4.17R$. The new reflection mode is derived from the horizontal mode, which is discussed in the following text. The reflection band of $P = 2.8R$ between $\lambda = 6.5R$ and $\lambda = 8R$ transforms into two reflection peaks of $P = 4R$. When the period further increases (Figure 3c), the perfect transmission peaks only exhibit marginal changes; however, all the perfect reflection peaks in the range of $\lambda < P$ disappear. For example, when $P = 5R$ (black solid curve in Figure 3c), all the perfect reflection peaks below $\lambda = 5R$ disappear, whereas when

$P = 7R$ (red dotted curve in Figure 3c), all the perfect reflection peaks below $\lambda = 7R$ disappear. Hence, there must exist different mechanisms for the generation of transmission and reflection peaks. The preliminary results indicate that reflection peaks depend mainly on lattice coupling, and the metasurface can generate perfect reflection peaks only when the incident wavelength is longer than its period. By contrast, transmission peaks appear to be independent of lattice coupling; however, these peaks are influenced by multipolar interference.

For s-polarized (TE) incident waves (Figure 3b,d), the peaks in the short wavelength region degrade when the period increases. Moreover, a new mode at $\lambda = 6.47R$ (marked by red dashed circle in Figure 3b) appears when $P = 4R$ (blue dashed line in Figure 3b). This new mode is also derived from the horizontal mode, as depicted in the inset of Figure 3b. For $P = 5R$ (black solid curve in Figure 3d), no perfect reflection peaks

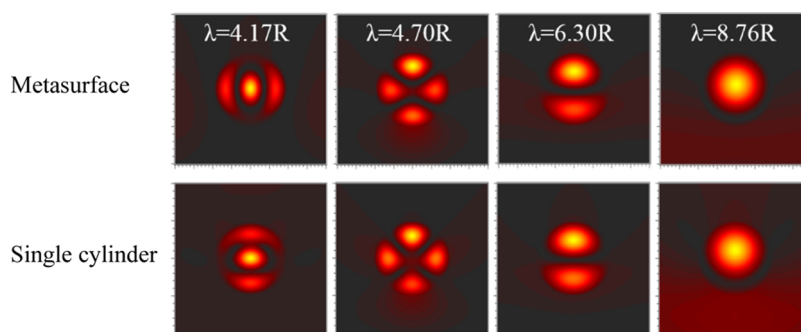


Figure 5. Four modes of the reflection peaks of $P = 4R$ when $n = 3.6$ at $\lambda = 4.17R$, $4.70R$, $6.3R$, and $8.76R$ (top row). The four modes at corresponding wavelengths of the single cylinder (bottom row).

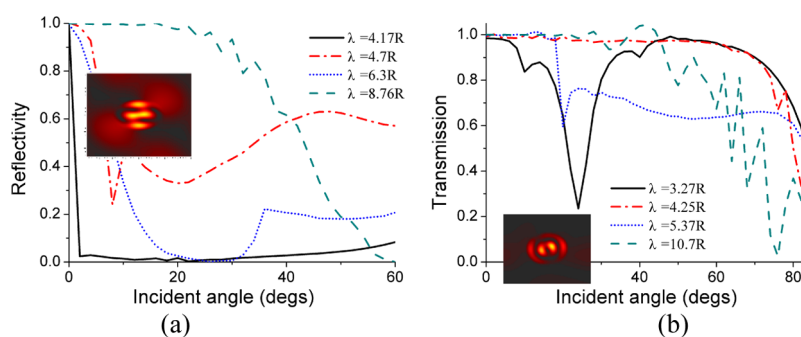


Figure 6. Incident angles of optical waves (Φ) affect the (a) reflection and (b) transmission properties at different peaks of $P = 4R$ when $n = 3.6$.

exist below $\lambda = 5R$, whereas for $P = 7R$ (red dotted curve in Figure 3d), no perfect reflection peaks exist below $\lambda = 7R$. The results obtained for TE waves are similar to those obtained for TM waves. The characteristics of p- and s-polarized incident waves are similar. Hence, we mainly focus on p-polarized (TM) incident waves in the following text.

The optical modes (patterns) at each transmission and reflection peak associated with different periods are displayed in Figure 4. The optical patterns exhibit little change with the period. In the long wavelength region, the optical field is basically the single mode. As the wavelength moves to the short wave direction, higher order modes begin to appear. The distribution of most of these optical modes is basically the same as that of a single cylinder (Figure 5). In Figure 5, four modes of the reflection peaks of $P = 4R$ at $\lambda = 4.17R$, $4.70R$, $6.3R$, and $8.76R$ are illustrated in the top row; the corresponding modes of a single cylinder are displayed in the bottom row for comparison. At $\lambda = 4.70R$, $6.3R$, and $8.76R$, the modes of the metasurface and single cylinder are identical. The modes mainly depend on the relative size of the wavelength and cylinder (called “vertical modes” because the optical field exhibits a vertical distribution). The vertical modes in the cylinder appear when the effective wavelength (λ/nR) in the media matches the wavelength of the electric dipole, EQ, and EO. Shorter wavelengths form higher order modes. Only the mode originating from the periodicity ($\lambda = 4.17R$) is different. This mode is transformed from a “vertical mode” to a “horizontal mode” (the optical field is distributed in the horizontal direction). Notably, no perfect reflection peaks are observed for the single cylinder. However, the vertical mode distributions of the single cylinder are similar to those of the metasurface, signifying that the perfect reflection or transmission peaks of vertical modes cannot be distinguished from optical field distributions. Moreover, the physical mechanisms

of the formation of perfect reflection peaks can be classified into two types. The first type of mechanism does not change the vertical optical mode distribution, whereas the other type changes the vertical mode into the horizontal mode.

The reflection properties of the four peaks displayed in Figure 5 are investigated. The reflection properties change dramatically as the incident angle (Φ) increases (Figure 6a). In particular, the peak of $\lambda = 4.17R$ (black solid line) is a perfect reflection point only when $\Phi = 0^\circ$. When $\Phi = 2^\circ$, the reflection value of the peak decreases sharply from 1 to nearly 0. Moreover, the horizontal mode is transformed back into a vertical mode (illustrated in the inset of Figure 6a), which also demonstrates that the horizontal mode is completely different from the vertical mode. As Φ increases, the other three perfect reflection points of the vertical modes also degenerate but at lower speeds than the peak of $\lambda = 4.17R$. For $\lambda = 8.76R$ (green dashed line), the reflection begins to drop after $\Phi = 20^\circ$. Moreover, the reflection decreases with some fluctuations, especially for $\lambda = 4.7R$ (red dashed line) and $\lambda = 6.3R$ (blue dotted line).

Transmission peaks also degenerate as Φ increases; however, they degenerate at a considerably lower speed than do reflection peaks (Figure 6b), which demonstrates that the mechanism of transmission peaks is different from that of reflection peaks. All the reflection peaks decrease in magnitude before the incident angle reaches approximately 20° . However, some transmission peaks begin to decline only when the incident angle is higher than 60° , such as the peak at $\lambda = 4.25R$ (red dashed line). For $\lambda = 3.27R$ (black solid line), the transmission peak declines after $\Phi = 10^\circ$; nevertheless, this peak again becomes a perfect transmission peak when Φ increases to approximately 45° , and perfect transmission is maintained until $\Phi > 60^\circ$, which is different from the behavior of other peaks. The reason for the valley at $\Phi = 24^\circ$ is the

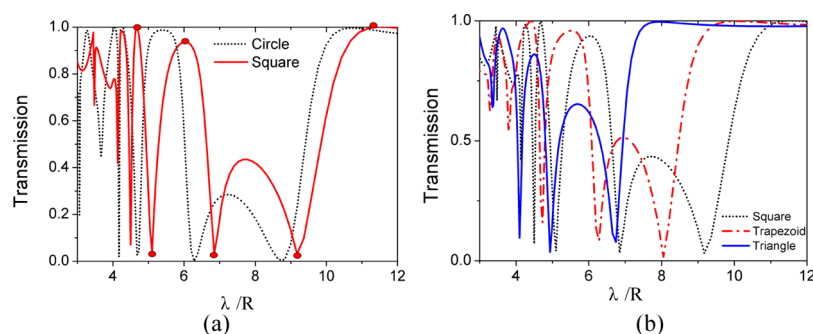


Figure 7. Transmission properties of different cross-sectional shapes at $P = 4R$ when $n = 3.6$: (a) circle (black dotted line) and square with a side length of $2R$ (red solid line) and (b) square (black dotted line), trapezoid with a top and bottom length of R and $2R$ (red dashed line), respectively, and triangle with a side length of $2R$ (blue solid line).

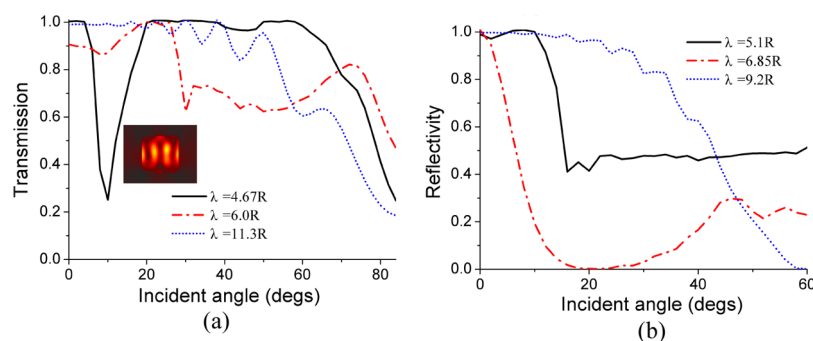


Figure 8. Change in the (a) transmission and (b) reflection characteristics with the incident angle (Φ). The period of the square metasurface is $4R$, the side length of the square is $2R$, and $n = 3.6$.

formation of a similar horizontal mode (not perfect), as displayed in the inset of Figure 6b. Here, the effective period changes to $P \cos \Phi \approx 3.6R$, which is close to the wavelength of $\lambda = 3.27R$, and the horizontal mode transforms back very rapidly with a change in Φ . Therefore, the horizontal mode forms when $\lambda \approx P$ and is sensitive to the light incident angle (Φ). This method can be applied for some practical applications, including high-efficiency tunable devices and antireflection.^{45,46}

The cross-sectional shape of the metasurface (square, trapezoidal, or even triangular) can also affect its properties (Figure 7). The shape of the transmission curve of the square section is similar to that of the transmission curve of the cylindrical section, but the square section exhibits a red shift (peaks marked by red dots; Figure 7a). All the peak values for the trapezoidal (red dashed line in Figure 7b) and triangular cross sections (blue solid line in Figure 7b) have different degrees of the blue shift and degradation compared with those observed for the square cross section (black dotted line in Figure 7b).

The up and down trapezoids and triangles have the same properties. Therefore, the circular or square metasurface is suitable for perfect transmission and reflection. The transmission and reflection peaks of the square metasurface (marked by the red dots in Figure 7a) have similar properties when the incident angle (Φ) changes, as displayed in Figure 8a,b, respectively.

When $\lambda = 4.67R$ (black solid line in Figure 8a, a transmission valley occurs at $\Phi = 10^\circ$ because of the horizontal mode, as illustrated in the inset of Figure 8a. When $\lambda = 6R$ (red dashed line in Figure 8a), the perfect transmission peak appears at $\Phi = 20^\circ$ and not at vertical incidence ($\Phi = 0^\circ$), which demonstrates

that the degenerated peaks at $\Phi = 0^\circ$ may become the perfect transmission peak again at some oblique incidence angles when the perfect multipolar interference condition is satisfied. When $\lambda = 11.3R$ (blue dotted line in Figure 8a), the transmission peak declines slowly, similar to the decline for the cylindrical metasurface. The three reflection peaks at $\lambda = 5.1R$ (black solid line in Figure 8b), $\lambda = 6.85R$ (red dashed line in Figure 8b), and $\lambda = 9.2R$ (blue dotted line in Figure 8b) exhibit properties similar to those of the corresponding reflection peaks of the cylindrical metasurface.

The advantage of the square metasurface is that the processing technology of the structure is relatively simple, which makes it more practical than the other metasurfaces. We also determine the transmission curve for a square surface structure on a dielectric film of $n = 1.4$ (Figure 9). The dielectric film does not change the shape of the transmission

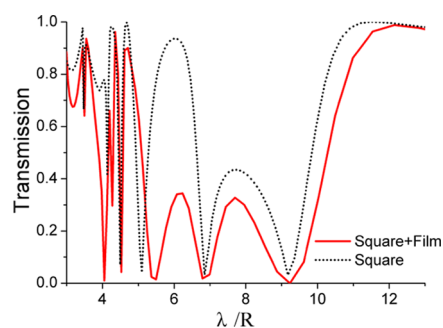


Figure 9. Transmission properties of a square metasurface (black dotted line) and a square metasurface on a dielectric film of $n = 1.4$ (red solid line).

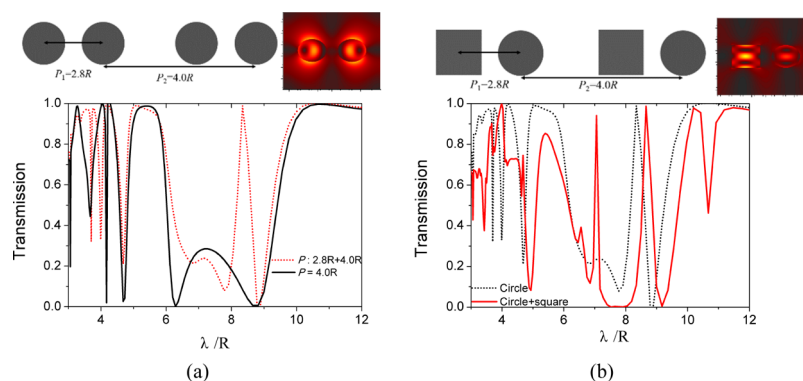


Figure 10. Transmission properties of hybrid periods and cross sections when $n = 3.6$: (a) circular metasurface with a period of $4R$ (black solid line) and hybrid periods of $2.8R$ and $4R$ (red dotted line) and (b) circular metasurface with hybrid periods of $2.8R$ and $4R$ (black dotted line) as well as hybrid circular and square metasurfaces with hybrid periods of $2.8R$ and $4R$ (red solid line). The insets of Figure 10a,b illustrate the corresponding schematic of the hybrid metasurface and the optical field distribution of the new generated transmission modes, respectively.

curve; however, it weakens the transmission peaks and enhances the reflection peaks. Hence, we can easily fabricate such a metasurface on a dielectric film to obtain perfect reflections at a designed frequency.

Metasurfaces with hybrid periods or hybrid cross sections can generate more transmission modes because they can meet more types of multipolar interference conditions, compared with other metasurfaces. For example, compared with a metasurface with a period of $P = 4R$ (black solid line in Figure 10a), a metasurface with hybrid periods of $P_1 = 2.8R$ and $P_2 = 4R$ (displayed in the inset of Figure 10a) generates a new transmission mode at $\lambda = 8.34R$ (red dotted line in Figure 10a). The optical mode distribution around two cylinders of P_1 is illustrated in the inset of Figure 10a, which displays a strong coupling interference mode. If one of the two circular cylinders of P_1 are changed to a square cylinder (inset of Figure 10b), we can obtain another new transmission mode at $\lambda = 7.06R$ (red solid line in the inset in Figure 10b). According to the optical field distribution displayed in the insets of Figure 10a,b, hybrid cross sections generate different multipolar interferences, which cause new transmission modes.

Another method of generating a new transmission mode is to use two or more metasurface layers. Changing the distance (D) between the two cylindrical metasurface layers can increase the order of the transmission mode (Figure 11). For example, when $D = 2.8R$ (red dashed line), a new transmission mode appears at $\lambda = 8.4R$. However, when the distance is sufficiently large, such as when $D = 5R$ (green dotted line), the interaction between the two layers can be neglected, and the

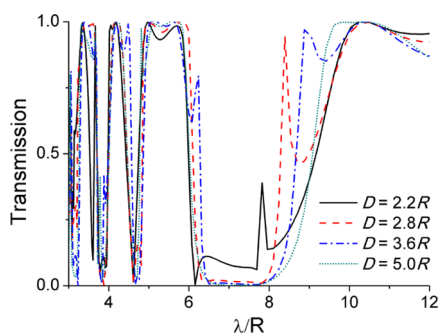


Figure 11. Different distances between two cylindrical metasurface layers. For each metasurface layer, $P = 4R$ and $n = 3.6$.

new mode disappears. No new perfect reflection mode appears under these conditions, which demonstrates that perfect reflection does not originate from multipolar interferences but from lattice coupling.

3. CONCLUSIONS

In conclusion, we investigate the mechanisms of perfect transmission and reflection in different metasurfaces. First, a change in the refractive index mainly changes the working frequency range of the metasurface through a change in the effective wavelength. Second, perfect reflections are strongly influenced by the period of metasurfaces and occur only when the period is less than the incident wavelength, which can be attributed to the lattice coupling. Lattice coupling can be divided into two types: vertical and horizontal mode coupling. The vertical mode appears when the effective wavelength (λ/nR) matches the feature size, whereas the horizontal mode only appears when the incident wavelength is close to the period. In particular, the horizontal mode is very sensitive to the incident angle, and the reflection peak can be changed into a transmission peak within 2° . By contrast, transmission peaks appear to be independent of lattice coupling because they basically remain unchanged as the period changes. However, we can increase the transmission modes by using hybrid periods, hybrid cross sections, or multilayers with different multipolar interferences. Therefore, we can easily control and obtain the properties of metasurfaces according to actual demands. Moreover, the properties of metasurfaces with square cross sections are as good as those of cylindrical metasurfaces, which can enable further practical applications of metasurfaces in optical beam control.

AUTHOR INFORMATION

Corresponding Author

*E-mail: jianglan@bit.edu.cn

ORCID

Lan Jiang: 0000-0003-0488-1987

YongFeng Lu: 0000-0002-5942-1999

Notes

The authors declare no competing financial interest.

ACKNOWLEDGMENTS

This study was supported by the National Natural Science Foundation of China (NSFC) under grant no. 61605140 and

the National Key R&D Program of China (2017YFB1104300), and Beijing Institute of Technology Research Fund Program for Young Scholars.

REFERENCES

- (1) Holloway, C. L.; Kuester, E. F.; Gordon, J. A.; O'Hara, J.; Booth, J.; Smith, D. R. An Overview of the Theory and Applications of Metasurfaces: The Two-Dimensional Equivalents of Metamaterials. *IEEE Antennas Propag. Mag.* **2012**, *54*, 10–35.
- (2) Kildishev, A. V.; Boltasseva, A.; Shalae, V. M. Planar photonics with metasurfaces. *Science* **2013**, *339*, 1232009.
- (3) Yu, N.; Capasso, F. Flat optics with designer metasurfaces. *Nat. Mater.* **2014**, *13*, 139–150.
- (4) Brongersma, M. L.; Cui, Y.; Fan, S. Light management for photovoltaics using high-index nanostructures. *Nat. Mater.* **2014**, *13*, 451.
- (5) Estakhri, N. M.; Alù, A. Recent progress in gradient metasurfaces. *J. Opt. Soc. Am. B* **2016**, *33*, A21–A30.
- (6) Zhang, L.; Mei, S.; Huang, K.; Qiu, C.-W. Advances in Full Control of Electromagnetic Waves with Metasurfaces. *Adv. Opt. Mater.* **2016**, *4*, 818–833.
- (7) Glybovski, S. B.; Tretyakov, S. A.; Belov, P. A.; Kivshar, Y. S.; Simovski, C. R. Metasurfaces: From microwaves to visible. *Phys. Rep.* **2016**, *634*, 1–72.
- (8) Chen, H.-T.; Taylor, A. J.; Yu, N. A Review of Metasurfaces: Physics and Applications. *Rep. Prog. Phys.* **2016**, *79*, 076401.
- (9) Genevet, P.; Capasso, F.; Aieta, F.; Khorasaninejad, M.; Devlin, R. Recent Advances in Planar Optics: From Plasmonic to Dielectric Metasurfaces. *Optica* **2017**, *4*, 139–152.
- (10) Ding, F.; Pors, A.; Bozhevolnyi, S. I. Gradient Metasurfaces: A Review of Fundamentals and Applications. *Rep. Prog. Phys.* **2018**, *81*, 026401.
- (11) Smirnova, D.; Kivshar, Y. S. Multipolar Nonlinear Nanophotonics. *Optica* **2016**, *3*, 1241–1255.
- (12) Li, G.; Zhang, S.; Zentgraf, T. Nonlinear Photonic Metasurfaces. *Nat. Rev. Mater.* **2017**, *2*, 17010.
- (13) Krasnok, A.; Tymchenko, M.; Alù, A. Nonlinear Metasurfaces: A Paradigm Shift in Nonlinear Optics. *Mater. Today* **2018**, *21*, 8.
- (14) Campione, S.; Guclu, C.; Ragan, R.; Capolino, F. Enhanced Magnetic and Electric Fields via Fano Resonances in Metasurfaces of Circular Clusters of Plasmonic Nanoparticles. *ACS Photonics* **2014**, *1*, 254–260.
- (15) Tretyakov, S. A. Metasurfaces for General Transformations of Electromagnetic Fields. *Philos. Trans. R. Soc., A* **2015**, *373*, 20140362.
- (16) Lalanne, P.; Chavel, P. Metalenses at visible wavelengths: past, present, perspectives. *Laser Photonics Rev.* **2017**, *11*, 1600295.
- (17) Yu, N.; Genevet, P.; Kats, M. A.; Aieta, F.; Tetienne, J.-P.; Capasso, F.; Gaburro, Z. Light Propagation with Phase Discontinuities: Generalized Laws of Reflection and Refraction. *Science* **2011**, *334*, 333.
- (18) Wilczek, F.; Shapere, A. *Geometric Phases in Physics*; World Scientific, 1989; Vol. 5.
- (19) Lin, D.; Fan, P.; Hasman, E.; Brongersma, M. L. Dielectric gradient metasurface optical elements. *Science* **2014**, *345*, 298–302.
- (20) Bliokh, K. Y.; Rodríguez-Fortuño, F. J.; Nori, F.; Zayats, A. V. Spin-orbit interactions of light. *Nat. Photonics* **2015**, *9*, 796–808.
- (21) Maguid, E.; Yulevich, I.; Yannai, M.; Kleiner, V.; L Brongersma, M.; Hasman, E. Multifunctional Interleaved Geometric-Phase Dielectric Metasurfaces. *Light: Sci. Appl.* **2017**, *6*, No. e17027.
- (22) Bao, L.; Ma, Q.; Bai, G. D.; Jing, H. B.; Wu, R. Y.; Fu, X.; Yang, C.; Wu, J.; Cui, T. J. Design of digital coding metasurfaces with independent controls of phase and amplitude responses. *Appl. Phys. Lett.* **2018**, *113*, 063502.
- (23) Zhang, X. G.; Jiang, W. X.; Tian, H. W.; Cui, T. J. Controlling Radiation Beams by Low-Profile Planar Antenna Arrays with Coding Elements. *ACS Omega* **2018**, *3*, 10601–10611.
- (24) Pfeiffer, C.; Grbic, A. Metamaterial Huygens' Surfaces: Tailoring Wave Fronts with Reflectionless Sheets. *Phys. Rev. Lett.* **2013**, *110*, 197401.
- (25) Estakhri, N. M.; Alù, A. Wave-Front Transformation with Gradient Metasurfaces. *Phys. Rev. X* **2016**, *6*, 041008.
- (26) Díaz-Rubio, A.; Asadchy, V. S.; Elsakka, A.; Tretyakov, S. A. From the Generalized Reflection Law to the Realization of Perfect Anomalous Reflectors. *Sci. Adv.* **2017**, *3*, No. e1602714.
- (27) Epstein, A.; Eleftheriades, G. V. Synthesis of Passive Lossless Metasurfaces Using Auxiliary Fields for Reflectionless Beam Splitting and Perfect Reflection. *Phys. Rev. Lett.* **2016**, *117*, 256103.
- (28) Yang, J.; Fan, J. A. Topology-Optimized Metasurfaces: Impact of Initial Geometric Layout. *Opt. Lett.* **2017**, *42*, 3161–3164.
- (29) Lin, Z.; Groever, B.; Capasso, F.; Rodriguez, A. W.; Lončar, M. Topology Optimized Multi-layered Meta-optics. **2017**, arXiv:1706.06715.
- (30) Cambiasso, J.; König, M.; Cortés, E.; Schlücker, S.; Maier, S. A. Surface-Enhanced Spectroscopies of a Molecular Monolayer in an All-Dielectric Nanoantenna. *ACS Photonics* **2018**, *5*, 1546–1557.
- (31) Sugimoto, H.; Fujii, M. Broadband Dielectric-Metal Hybrid Nanoantenna: Silicon Nanoparticle on a Mirror. *ACS Photonics* **2018**, *5*, 1986–1993.
- (32) Vaskin, A.; Bohn, J.; Chong, K. E.; Bucher, T.; Zilk, M.; Choi, D.-Y.; Neshev, D. N.; Kivshar, Y. S.; Pertsch, T.; Staude, I. Directional and Spectral Shaping of Light Emission with Mie-Resonant Silicon Nanoantenna Arrays. *ACS Photonics* **2018**, *5*, 1359–1364.
- (33) Wu, A.; Li, H.; Du, J.; Ni, X.; Ye, Z.; Wang, Y.; Sheng, Z.; Zou, S.; Gan, F.; Zhang, X.; Wang, X. Experimental Demonstration of In-Plane Negative-Angle Refraction with an Array of Silicon Nanoposts. *Nano Lett.* **2015**, *15*, 2055–2060.
- (34) Lin, D.; Melli, M.; Poliakov, E.; Hilaire, P. S.; Dhuey, S.; Peroz, C.; Cabrini, S.; Brongersma, M.; Klug, M. Optical Metasurfaces for High Angle Steering at Visible Wavelengths. *Sci. Rep.* **2017**, *7*, 2286.
- (35) Paniagua-Dominguez, R.; Yu, Y. F.; Khaidarov, E.; Bakker, R. M.; Liang, X.; Fu, Y. H.; Kuznetsov, A. I. A Metalens with Near-Unity Numerical Aperture. **2017**, arXiv:1705.00895.
- (36) Ra'di, Y.; Sounas, D. L.; Alù, A. Metagratings: Beyond the Limits of Graded Metasurfaces for Wave Front Control. *Phys. Rev. Lett.* **2017**, *119*, 067404.
- (37) Chalabi, H.; Ra'di, Y.; Sounas, D. L.; Alù, A. Efficient Anomalous Reflection through Near-Field Interactions in Metasurfaces. *Phys. Rev. B: Condens. Matter Mater. Phys.* **2017**, *96*, 075432.
- (38) Babicheva, V. E.; Evlyukhin, A. B. Resonant Lattice Kerker Effect in Metasurfaces With Electric and Magnetic Optical Responses. *Laser Photonics Rev.* **2017**, *11*, 1700132.
- (39) Khaidarov, E.; Hao, H.; Paniagua-Dominguez, R.; Yu, Y. F.; Fu, Y. H.; Valuckas, V.; Yap, S. L. K.; Toh, Y. T.; Ng, J. S. K.; Kuznetsov, A. I. Asymmetric Nanoantennas for Ultrahigh Angle Broadband Visible Light Bending. *Nano Lett.* **2017**, *17*, 6267.
- (40) Du, J.; Lin, Z.; Chui, S. T.; Lu, W.; Li, H.; Wu, A.; Sheng, Z.; Zi, J.; Wang, X.; Zou, S.; Gan, F. Optical Beam Steering Based on the Symmetry of Resonant Modes of Nanoparticles. *Phys. Rev. Lett.* **2011**, *106*, 203903.
- (41) Chang-Hasnain, C. J.; Yang, W. High-Contrast Gratings for Integrated Optoelectronics. *Adv. Opt. Photonics* **2012**, *4*, 379–440.
- (42) Collin, S. Nanostructure Arrays in Free-Space: Optical Properties and Applications. *Rep. Prog. Phys.* **2014**, *77*, 126402.
- (43) Vynck, K.; Felbacq, D.; Centeno, E.; Căbuz, A. I.; Cassagne, D.; Guizal, B. All-Dielectric Rod-Type Metamaterials at Optical Frequencies. *Phys. Rev. Lett.* **2009**, *102*, 133901.
- (44) Liu, W.; Miroshnichenko, A. E. Beam Steering with Dielectric Metalattices. *ACS Photonics* **2017**, *5*, 1733–1741.
- (45) Nemati, A.; Wang, Q.; Hong, M. H.; Teng, J. H. Tunable and reconfigurable metasurfaces and metadevices. *Opto-Electro. Adv.* **2018**, *1*, 18000901.
- (46) Yang, J.; Luo, F.; Kao, T. S.; Li, X.; Ho, G. W.; Teng, J.; Luo, X.; Hong, M. Design and fabrication of broadband ultralow reflectivity black Si surfaces by laser micro/nanoprocessing. *Light: Sci. Appl.* **2014**, *3*, No. e185.